

Independent Control of Microswimmers with a Uniform Magnetic Field

Lucas Amoudruz¹ and Petros Koumoutsakos^{1,2,*}

¹*Computational Science and Engineering Laboratory, ETH Zürich, CH-8092, Switzerland.*

²*John A. Paulson School of Engineering and Applied Sciences, Harvard University, Cambridge, MA, USA.*

(Dated: December 23, 2024)

Artificial bacteria flagella (ABFs) are magnetic helical micro-robots that can be remotely controlled via a uniform, rotating magnetic field. While the control of a single swimmer with the uniform magnetic field is straightforward, the independent control of multiple ABFs is an unsolved problem. We demonstrate such independent control by exploiting the distinct geometries of the ABFs through an analytical solution and a reinforcement learning algorithm. We compare the two algorithms and demonstrate the superiority of reinforcement learning in achieving multiple objectives. The results demonstrate, for the first time, effective independent navigation of realistic micro-swimmers in a viscous flow field. We argue that the present precise control strategies are readily applicable in the laboratory.

I. INTRODUCTION

The magnetic control of micro-swimming devices [1, 2] through micro-manipulation [3], targeted drug delivery [4] or convection-enhanced transport [5], has created new frontiers for bio-medicine. A particularly promising technology involves corkscrew-shaped magnetic micro-swimmers (artificial bacterial flagella (ABFs)) that propel themselves when subjected to a rotating magnetic field [6]. Rotating magnetic fields can form propulsive gradients and they are arguably preferable to alternatives, such as electric fields, for in-vivo conditions [7]. However, the independent, yet coordinated, control of individual ABFs is challenging as it requires balancing between the magnetic forces and the hydrodynamic interactions between the swimmers while the employed magnetic fields are practically uniform over lengths of few micrometers. We note that independent navigation of mm-sized micro-swimmers has been shown in [8] through experiments and simulations, while [9] a reinforcement learning (RL) algorithm was applied to adjust the velocity of an idealised swimmer in simulations with one way coupling with a complex flow field. Control of swimmers using two-way coupling and RL have been demonstrated with linked-spheres at low Reynolds numbers [10] and for artificial fish in macro-scales [11, 12]. To the best of our knowledge the independent control of two micron-sized swimmers in a magnetic field has not been reported before.

In this letter, we present two methods to independently guide two micro-ABFs towards a single target in the presence of a uniform magnetic field. The two methods rely on simulations of swimming ABFs using the method of Dissipative Particle Dynamics dissipative particle dynamics (DPD) [13, 14], taking into account the particular geometry of the swimmers and their interactions with the viscous fluid. We first present a semi-analytical solution for the simple yet instructive setup of

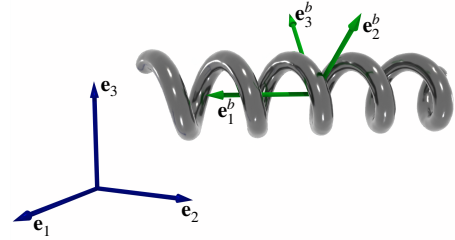


FIG. 1. The laboratory frame ($\mathbf{e}_1, \mathbf{e}_2, \mathbf{e}_3$) and the ABF body frame ($\mathbf{e}_1^b, \mathbf{e}_2^b, \mathbf{e}_3^b$). The ABF is aligned with its body frame so that the swimming direction is along \mathbf{e}_1^b .

multiple, geometrically distinct ABFs in free space, with zero background flow. This study enables understanding of the design constraints for the ABFs necessary for independent control and how their geometric characteristics relate to their travel time. We then employ RL to control multiple ABFs trajectories in a broad range of flow conditions including a non-zero background flow.

II. ARTIFICIAL BACTERIAL FLAGELLA

The ABFs are modeled as microscopic rigid bodies of length l with position \mathbf{r} and orientation q (represented by a quaternion), immersed in a viscous fluid and subjected to a rotating, uniform, magnetic field. We estimate that the magnetic and hydrodynamic interactions between ABFs are orders of magnitude smaller than those due to the magnetic field (see supplementary material (SM)) and we ignore inertial effects due to their low Reynolds number ($Re \approx 10^{-3}$). Following this approximation, the system is fully described by the position and orientation of the ABFs.

Additionally, the linear and angular velocities of the ABF, \mathbf{V}^b and $\boldsymbol{\Omega}^b$, are directly linked to the external force

* petros@seas.harvard.edu

and torque, \mathbf{F}^b and \mathbf{T}^b , via the *mobility matrix* [15],

$$\begin{bmatrix} \mathbf{V}^b \\ \boldsymbol{\Omega}^b \end{bmatrix} = \begin{bmatrix} \Delta & Z \\ Z^T & \Gamma \end{bmatrix} \begin{bmatrix} \mathbf{F}^b \\ \mathbf{T}^b \end{bmatrix}, \quad (1)$$

where the superscript b indicates that the quantity is expressed in the ABF frame of reference (fig. 1), for which Δ , Z and Γ are diagonal. The matrices Γ and Z represent the application of torque to changing the angular and linear velocity, respectively. The ABFs are propelled by torque applied through a magnetic field and we assume that it can swim only in the direction of its main axis so that Z has only one non-zero entry (Z_{11}). The coefficients in the mobility matrix are often estimated by empirical formulas for low Reynolds number flows [16]. Here we estimate the components of the mobility matrix for the specific ABF by conducting flow simulations using DPD [13, 14]. We remark that the shape (pitch, diameter, length) of the ABF influence the elements of these matrices (see SM) and the present approach allows to account for these geometries.

The ABF with a magnetic moment \mathbf{m} is subjected to a uniform magnetic field B and hence experiences a torque

$$\mathbf{T} = \mathbf{m} \times \mathbf{B}. \quad (2)$$

No other external force is applied to the ABF, hence $\mathbf{F} = \mathbf{0}$. Combining eq. (1) with the kinematic equations for a rigid body gives the following system of ordinary differential equation (ODE):

$$\dot{\mathbf{x}} = \mathbf{V}, \quad (3a)$$

$$\dot{q} = \frac{1}{2}q \otimes \hat{\boldsymbol{\Omega}} \quad (3b)$$

$$\mathbf{V}^b = Z\mathbf{T}^b, \quad (3c)$$

$$\boldsymbol{\Omega}^b = \Gamma\mathbf{T}^b, \quad (3d)$$

where \otimes denotes the quaternion product, and $\hat{\boldsymbol{\Omega}}$ the pure quaternion formed by the vector $\boldsymbol{\Omega}$. The transformations between the laboratory frame of reference and that of the ABF are given by:

$$\mathbf{T}^b = R(q)\mathbf{T}, \quad (4a)$$

$$\mathbf{m} = R(q^*)\mathbf{m}^b, \quad (4b)$$

$$\boldsymbol{\Omega} = R(q^*)\boldsymbol{\Omega}^b, \quad (4c)$$

$$\mathbf{V} = R(q^*)\mathbf{V}^b, \quad (4d)$$

where q^* is the conjugate of q and $R(q)$ is the rotation matrix that corresponds to the rotation by a quaternion q (see SM). The system of differential equations eqs. (2) and (3) is advanced in time with a fourth order Runge-Kutta integrator.

III. FORWARD VELOCITY

ABFs were designed to swim under a rotating, uniform magnetic field [6, 17]. We study this scenario by applying the field $\mathbf{B}(t) = B(0, \cos \omega t, \sin \omega t)$ to ABFs aligned

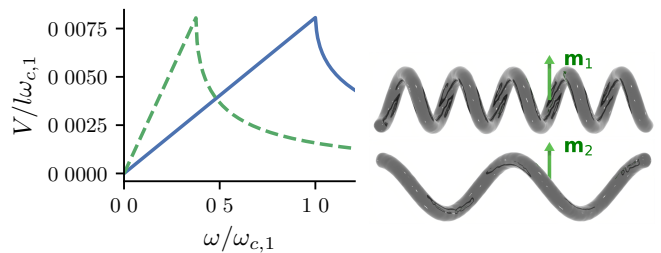


FIG. 2. Left: Dimensionless time averaged forward velocity of two ABFs, differing in shape and magnetic moment, against the field rotation frequency (in units of the step-out frequency of the first swimmer, $\omega_{c,1}$). Right: The ABFs geometries. The arrows represent the magnetic moment of the ABFs.

with the x axis of the laboratory frame. We consider two ABFs with the same length but different pitch and magnetic moments, as shown in fig. 2. The difference in pitch results in different coefficients of the mobility matrix and along with the different magnetic moments results in distinct propulsion velocities for the two ABFs. For each ABF velocity we distinguish a linear and a non-linear variation with respect to the frequency of the magnetic field. First, the ABF rotates at the same frequency as the magnetic field and its forward velocity increases linearly with the frequency of the magnetic field, consistent with the low Reynolds approximation [4, 18, 19]. In the non-linear regime, the magnetic torque is no longer able to sustain the same frequency of rotation as the magnetic field. The onset of non-linearity depends on the geometry and magnetic moment of the ABF as well as the imposed magnetic field. Indeed, the magnitude of the magnetic torque is bounded while that of the hydrodynamic torque increases linearly with the ABF angular velocity Ω . The torque imbalance at high rotation frequencies causes the ABF to slip resulting in an alternating forward and backward motion (see SM). Increasing the frequency further increases the effective slip and accordingly decreases the forward velocity. The two regimes are distinguished by the step-out frequency ω_c corresponding to the maximum forward velocity of the ABF.

The differences in propulsion velocities for the ABFs can be exploited to control independently their trajectories. The slope V/ω in the linear regime depends only on the shape of the ABF. The step-out frequency depends on both the shape and the magnetic moment (it can also be changed by varying the surface wettability of the ABF [20]). These two properties can be chosen such that the forward velocities of two ABFs react differently to the magnetic rotation frequency (fig. 2). By changing ω , it is then possible to control the relative velocities of the two ABFs: one is faster than the other in one regime while the opposite occurs in another regime. This simple observation constitutes the key idea for independent control of several ABFs even with a uniform magnetic field. We remark that, while this potential has been previously identified [18, 20], to the best of our knowledge, this is the

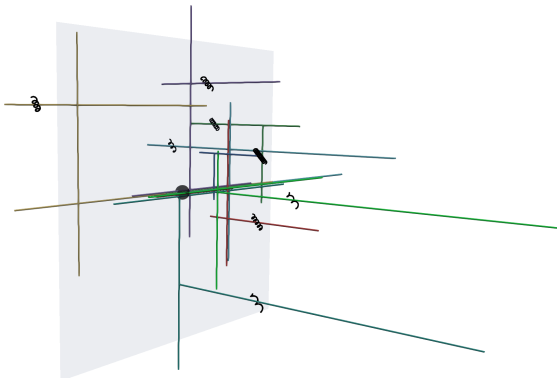


FIG. 3. Example trajectory of 8 swimmers obtained with the semi-analytical solution: The ABFs are first gathered on a plane, then on a line, and finally at the target (dark sphere). The ABFs drawn on the figure are located at their initial positions.

first time that such independent controlled navigation of multiple micro-swimmers is materialised.

IV. INDEPENDENT CONTROL I: SEMI-ANALYTICAL SOLUTION

In the absence of an external flow field, we derive a semi-analytical strategy for the navigation of N ABFs towards a particular target. Each ABF has a distinct magnetic moment and without any loss of generality, we set the target position of all swimmers to the origin and define the initial position of the i^{th} ABF as $\mathbf{x}^{(i)}$. We assume that the time required by one ABF to align with the rotation direction of the field is much smaller than $|\mathbf{x}^{(i)}|/v$, where v is the typical forward velocity of the ABF. The proposed strategy consists in gathering all ABFs along one direction \mathbf{n}_k at a time, such that $\mathbf{x}^{(i)} \cdot \mathbf{n}_k = 0$, $i = 1, 2, \dots, N$ after phase k . Hence, in three dimensions, the strategy consists of three phases, $k = 1, 2, 3$, until all ABFs have reached their target: they first gather on a plane, then on a line and finally to the target (fig. 3). We choose an alternating direction pathway such that $\mathbf{n}_i \cdot \mathbf{n}_j = \delta_{ij}$.

All ABFs are gathered along a given direction \mathbf{n} by exploiting the different forward responses of the ABFs when we alternate the frequency of rotation of the magnetic field. More specifically, for N ABFs, the field rotates for t_j time units at frequency $\omega_{c,j}$, $j = 1, 2, \dots, N$, where $\omega_{c,j}$ is the step-out frequency of the j^{th} swimmer. We define the *velocity matrix* with elements

$$U_{ij} = V_i(\omega_{c,j}),$$

denoting the velocity of swimmer i when the field rotates with the step out frequency of swimmer j . We can relate the above quantities to the (signed) distances d_j covered

by the ABFs as

$$d_i = \sum_{j=1}^N s_j t_j U_{ij},$$

where s_j determines if the field rotates clockwise/counterclockwise ($s_j = +1/-1$). Equivalently, the vector form of the above is

$$\mathbf{d} = U\beta, \quad (5)$$

where $\beta_j = t_j s_j$. Setting $d_i = \mathbf{x}^{(i)} \cdot \mathbf{n}$, we can invert eq. (5) and obtain the times spent at each step-out frequency

$$\beta = U^{-1}X\mathbf{n},$$

where we have set $X_{ij} = x_j^{(i)}$. Therefore, the total time spent at phase k is given by

$$T(\mathbf{n}_k) = \sum_{i=1}^N t_i = \sum_{i=1}^N |\beta_i| = \|U^{-1}X\mathbf{n}_k\|_1.$$

The yet unknown directions are chosen such that the total time is minimized. These directions are orthonormal and can thus be written as $\mathbf{n}_k = R(\phi, \theta, \psi)\mathbf{e}_k$, $k = 1, 2, 3$, where $R(\phi, \theta, \psi)$ is the rotation matrix given by the three Euler angles ϕ , θ and ψ . The optimal angles satisfy

$$\phi^*, \theta^*, \psi^* = \arg \min_{\phi, \theta, \psi} \sum_{k=1}^3 T(R(\phi, \theta, \psi)\mathbf{e}_k).$$

We solve the above minimization problem numerically with derandomized evolution strategy with covariance matrix adaptation (CMA-ES) [21].

V. INDEPENDENT CONTROL II: REINFORCEMENT LEARNING

We now employ a RL approach to solve the problem introduced in section IV. Each of the N ABFs is initially placed at a random position $\mathbf{x}_i \sim \mathcal{N}(\mathbf{x}_i^0, \sigma)$, $i = 1, 2, \dots, N$. The RL agent controls the magnetic field and has the goal of bringing all ABFs within a small distance (here two body lengths, $d = 2l$) from the target origin. This small distance is justified by the assumption of non-interacting ABFs. The agent sets the direction and magnitude of the magnetic field frequency every fixed time interval. An episode is terminated if either of the two conditions occur: (a) all ABFs reached the target within a small distance d , or (b) the simulation time exceeds a maximum time T_{\max} . The positions \mathbf{x}_i and orientations q_i of the ABFs describe the state s of the environment in the RL framework. The action performed by the agent every Δt time encodes the magnetic field rotation frequency and orientation for the next time interval. The reward of the system is designed so that all ABFs reach the target and the travel time is minimized.

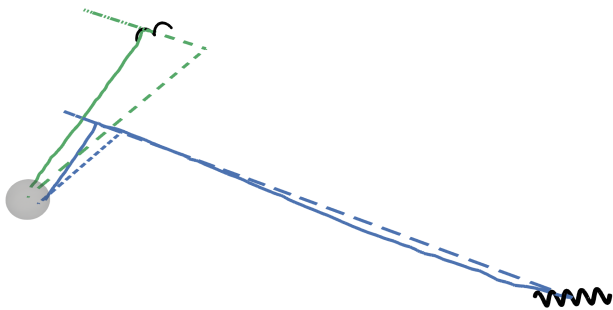


FIG. 4. Trajectories of the ABFs from their initial positions (ABF representations) to the target area (sphere) obtained with the two methods: semi-analytical (dashed lines) and RL (solid lines). The size of the ABFs has been scaled up by a factor of 7, for visualization purpose.

Additionally, a shaping reward term [22] is added to improve the learning process. The training is performed using VRACER, the off-policy actor critic RL method described in [23, 24]. More details on the RL setup are available in the SM.

VI. REACHING THE TARGETS

In this section, we demonstrate the effectiveness of the two methods introduced in sections IV and V. We first consider 2 ABFs in free space with zero background flow. Figure 5 shows the distance of the ABFs to their target over time, and the corresponding magnetic field rotation frequency for both methods. In both cases, the ABFs successfully reach their target. Interestingly, the rotation frequencies chosen by the RL agent correspond to the step-out frequencies of the ABFs. Indeed, these frequencies allow the fastest absolute velocity difference between the ABFs, so it is intuitively consistent that they are part of the fastest solution found by the RL method. Furthermore, the RL trained swimmer was about 25% faster than the semi-analytical swimmer. Furthermore we remark that the RL solution amounts to first blocking the forward motion of one swimmer while the other continues swimming (see fig. 4). The blocked swimmer is first reoriented such that its swimming direction is contained in the plane of the magnetic field rotation. On the other hand, the method presented in section IV makes both swimmers swim at all time, even if one of them must go further from its target. In such situations, the “blocking” method found by RL is advantageous over the other method.

We now compare the two methods in the case of 2 ABFs swimming in a background flow with non zero velocity. The assumptions required for deriving the semi-analytical approach are violated and the results is simply shown for comparison.

In the presence of a background flow the eq. (4d) be-

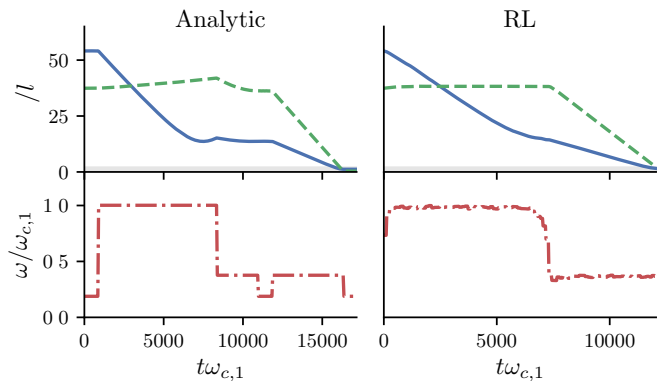


FIG. 5. Distance to target of the two controlled ABFs (in units of body length l) against dimensionless time (— and - - -) in free space, zero background flow, and corresponding magnetic field rotation frequency (— · —), where $\omega_{c,1}$ is the step-out frequency of the first swimmer.

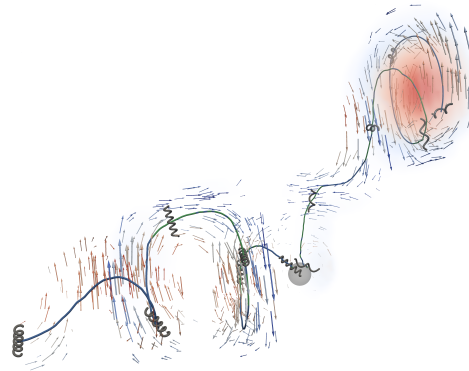


FIG. 6. Trajectories of the ABFs with non-zero flow obtained with the RL method. The arrows represent the velocity field and the colors represent the magnitude of the vorticity field. The flow field is only shown for a distance less than $4l$ from the trajectories, where l is the length of the swimmers.

comes

$$\mathbf{V} = R(q^*)\mathbf{V}^b + \mathbf{u}_\infty(\mathbf{x}),$$

where \mathbf{u}_∞ is the background velocity field. The background flow does not change in time and is set to the initial conditions of the Taylor-Green vortex,

$$\mathbf{u}_\infty(\mathbf{r}) = \begin{bmatrix} A \cos ax \sin by \sin cz \\ B \sin ax \cos by \sin cz \\ C \sin ax \sin by \cos cz \end{bmatrix}. \quad (6)$$

with the divergence free constrain $Aa + Bb + Cc = 0$. We choose here $A = B = C/2 = V$ and $a = b = -c = 2\pi/50l$.

The distances between the swimmers and the target over time are shown for both methods on fig. 7 demonstrating the expected divergence of the semi-analytical

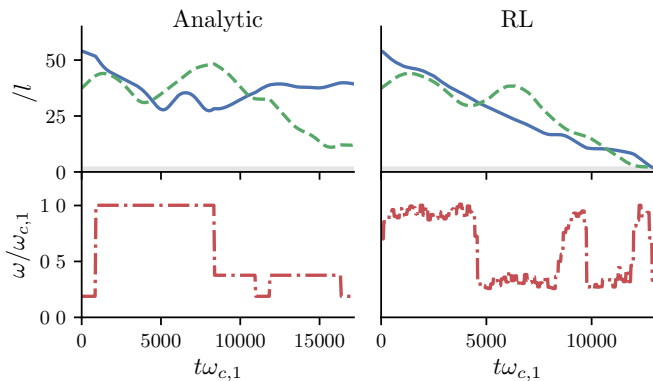


FIG. 7. Distance to target of the two controlled ABFs (in units of body length l) against dimensionless time (— and - - -) in free space with the background flow described by eq. (6) and corresponding magnetic field rotation frequency (— · —), where $\omega_{c,1}$ is the step-out frequency of the first swimmer.

method. On the other hand, the RL method successfully navigates the ABFs to their target. The magnetic action space exhibits a richer behavior than in the free space case. The rotation frequency of the magnetic field seems to oscillate between the step out frequencies of both swimmers and never exceeds the highest of these frequencies, where the swimming performance would degrade considerably. Furthermore, the trajectory seems to make use of the velocity field to achieve a lower travel time: fig. 6 shows that the trajectories tend to be parallel to the velocity field. The RL method not only found a solution, but also made use of its environment to make the control efficient.

Finally, we test the robustness of the RL method to flow variations. A perturbation $\delta\mathbf{u}(\mathbf{r}) = \varepsilon\mathbf{u}_\infty(\mathbf{r}/p)$ is added to the background flow described in eq. (6), where ε controls the strength of the perturbation and p controls the wave length of the perturbation with respect to the original one.

Figure 8 shows the success rate (number of trajectories that reached the target divided by the number of tries) against the perturbation strength ε for different wave-lengths. For large wave lengths ($p \geq 1$), the RL agent is able to successfully navigate the ABFs to their target in more than 90% when the perturbation strengths of less than 20%. However, the success rate degrades more sharply for smaller wave lengths ($p < 1$). Interestingly, when the wave length of the perturbation is the same as that of the training background flow ($p = 1$), the RL agent is successful in more than 30% of the cases even for large perturbations.

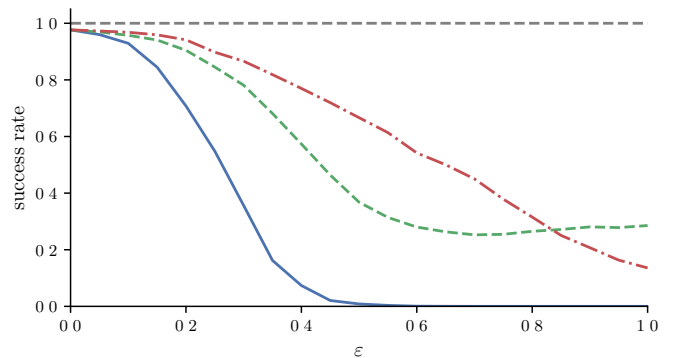


FIG. 8. Success rate of the RL method to guide swimmers to the target against the flow perturbation strength ε , for different wave numbers, $p = 1/2$ (—), $p = 1$ (- - -), $p = 2$ (— · —).

VII. SUMMARY

We have presented two methods to guide multiple ABFs individually towards targets with a uniform magnetic field. The semi-analytical method allows to understand the basic mechanisms that allow independent control and we derive the necessary condition for the independent control of multiple ABFs: their velocity matrix must be invertible, a condition that can be accommodated by suitably choosing the geometries of the swimmers. This result may further help to optimize the shapes of ABFs to further reduce the travel time.

The RL approach can control multiple ABFs in quiescent as well as in the presence of a complex background flow and is resilient to small flow perturbations. When the background flow vanishes, the RL method recovers a very similar behavior as the first method: the rotation frequency is alternating between the step-out frequencies of the swimmers. Furthermore, the RL method could reach lower travel time than the first method by blocking one swimmer while the other is swimming.

The current work focused on the simplified case of non-interacting swimmers. In practice, the ABFs may interact hydrodynamically and magnetically with each other, encounter obstacles, evolve in confined geometries or experience time varying flows. Nevertheless, we expect the RL method to be a good candidate to overcome these variants, in the same way as it naturally handled the addition of a background flow.

ACKNOWLEDGMENTS

We acknowledge insightful discussions with Guido Novati (ETHZ) and his technical support for the usage of `smarties`. We acknowledge support by the European Research Council (ERC Advanced Grant 341117).

-
- [1] Q. Cao, X. Han, and L. Li, *Lab Chip* **14**, 2762 (2014).
- [2] L. Yang and L. Zhang, *Annual Review of Control, Robotics, and Autonomous Systems* **4**, null (2021), <https://doi.org/10.1146/annurev-control-032720-104318>.
- [3] L. Zhang, K. E. Peyer, and B. J. Nelson, *Lab on a Chip* **10**, 2203 (2010).
- [4] R. Mhanna, F. Qiu, L. Zhang, Y. Ding, K. Sugihara, M. Zenobi-Wong, and B. J. Nelson, *Small* **10**, 1953 (2014).
- [5] S. Schuerle, A. P. Soleimany, T. Yeh, G. M. Anand, M. Häberli, H. E. Fleming, N. Mirkhani, F. Qiu, S. Hauert, X. Wang, B. J. Nelson, and S. N. Bhatia, *Science Advances* **5**, 1 (2019).
- [6] L. Zhang, J. J. Abbott, L. Dong, B. E. Kratochvil, D. Bell, and B. J. Nelson, *Applied Physics Letters* **94**, 064107 (2009).
- [7] H. Gu, Q. Boehler, D. Ahmed, and B. J. Nelson, *Science Robotics* **4**, 10.1126/scirobotics.aax8977 (2019).
- [8] D. Wong, E. B. Steager, and V. Kumar, *IEEE Robotics and Automation Letters* **1**, 554 (2016).
- [9] S. Colabrese, K. Gustavsson, A. Celani, and L. Biferale, *Physical Review Letters* **118**, 1 (2017).
- [10] A. C. H. Tsang, P. W. Tong, S. Nallan, and O. S. Pak, *Phys. Rev. Fluids* **5**, 074101 (2020).
- [11] M. Gazzola, B. Hejazialhosseini, and P. Koumoutsakos, *SIAM Journal on Scientific Computing* **36**, 622 (2014).
- [12] S. Verma, G. Novati, and P. Koumoutsakos, *Proceedings of the National Academy of Sciences of the United States of America* **115**, 5849 (2018).
- [13] P. Espanol and P. Warren, *EPL (Europhysics Letters)* **30**, 191 (1995).
- [14] D. Alexeev, L. Amoudruz, S. Litvinov, and P. Koumoutsakos, *Comput. Phys. Commun.* , 107298 (2020).
- [15] J. Happel and H. Brenner, *Low Reynolds number hydrodynamics: with special applications to particulate media*, Vol. 1 (Springer Science & Business Media, 1981).
- [16] S. Kim and S. J. Karrila, *Microhydrodynamics: principles and selected applications* (Courier Corporation, 2013).
- [17] A. Ghosh and P. Fischer, *Nano letters* **9**, 2243 (2009).
- [18] K. E. Peyer, L. Zhang, and B. J. Nelson, *Nanoscale* **5**, 1259 (2013).
- [19] D. Li, M. Jeong, E. Oren, T. Yu, and T. Qiu, *Robotics* **8**, 87 (2019).
- [20] X. Wang, C. Hu, L. Schurz, C. De Marco, X. Chen, S. Pané, and B. J. Nelson, *ACS Nano* **12**, 6210 (2018).
- [21] N. Hansen, S. D. Müller, and P. Koumoutsakos, *Evolutionary computation* **11**, 1 (2003).
- [22] A. Y. Ng, D. Harada, and S. Russell, in *ICML*, Vol. 99 (1999) pp. 278–287.
- [23] G. Novati, L. Mahadevan, and P. Koumoutsakos, *Physical Review Fluids* **4**, 10.1103/PhysRevFluids.4.093902 (2019).
- [24] G. Novati and P. Koumoutsakos, in *Proceedings of the 36th International Conference on Machine Learning* (2019).

Supplementary Information: Independent Control of Microswimmers with a Uniform Magnetic Field

Lucas Amoudruz¹ and Petros Koumoutsakos^{1,2,*}

¹*Computational Science and Engineering Laboratory, ETH Zürich, CH-8092, Switzerland.*

²*John A. Paulson School of Engineering and Applied
Sciences, Harvard University, Cambridge, MA, USA.*

(Dated: December 23, 2024)

arXiv:2101.10628v1 [physics.flu-dyn] 26 Jan 2021

I. NEGLECTING THE INTERACTIONS BETWEEN SWIMMERS

The artificial bacterial flagella (ABFs) experience hydrodynamic drag forces and torques. Additionally, they are subjected to a magnetic torque from the external, imposed, magnetic field. Furthermore, when multiple swimmers compose the system, hydrodynamic and magnetic interactions occur. Here we estimate the magnitude of these interaction forces by considering a simplified representation of the ABFs immersed in a fluid of viscosity $\eta = 10^{-3}$ Pa s, subjected to a rotating magnetic field of magnitude $B = 1$ mT. To have a rough estimate of the hydrodynamic torque, we represent the ABFs as ellipsoidal bodies of size $2a \times 2b \times 2c = 10 \mu\text{m} \times 2 \mu\text{m} \times 2 \mu\text{m}$. The magnetic fields rotates with angular velocity $\omega = 10 \cdot 2\pi\text{s}^{-1}$ which is also the step-out frequency ω_c of the ABFs. These choices correspond to similar conditions as those found in experimental work for ABFs [1].

Considering the equivalent sphere of the ABF, with a radius $R = (abc)^{1/3}$, the hydrodynamic torque magnitude can be expressed as [2]

$$T_H = 8\pi\eta R^3\omega. \quad (1)$$

At the step out frequency, the magnetic torque reaches its maximum magnitude,

$$T_M = mB, \quad (2)$$

where m is the magnetic moment of the sphere. Equating eqs. (1) and (2) gives an estimate for the magnetic moment

$$m = \frac{8\pi\eta R^3\omega}{B}, \quad (3)$$

hence $m \approx 8 \times 10^{-15}$ Am².

The magnetic field generated by a dipole of moment \mathbf{m} is given by

$$\mathbf{B}_D(\mathbf{r}) = \frac{\mu_0}{4\pi r^3} (3(\mathbf{m} \cdot \hat{\mathbf{r}})\hat{\mathbf{r}} - \mathbf{m}), \quad (4)$$

where $\hat{\mathbf{r}} = \mathbf{r}/r$ and $r = |\mathbf{r}|$.

Therefore, the magnetic torque exerted by one sphere of moment \mathbf{m}_2 to another of moment \mathbf{m}_1 (separated by a distance r) is given by

$$\mathbf{T}_{DD}(\mathbf{r}) = \mathbf{m}_1 \times \mathbf{B}_D(\mathbf{r}) = \frac{\mu_0}{4\pi r^3} (3(\mathbf{m}_1 \cdot \hat{\mathbf{r}})(\mathbf{m}_2 \times \hat{\mathbf{r}}) - \mathbf{m}_1 \times \mathbf{m}_2). \quad (5)$$

* petros@ethz.ch

Considering a small distance between the spheres $r = 10a$ (five body lengths between the centers) and replacing with the numerical values, we obtain $T_{DD}/T_M \approx 10^{-5}$, hence we neglect the magnetic interactions between swimmers. Similarly, the magnetic force caused by the gradient of the magnetic field generated by the dipole is negligible compared to that of the hydrodynamic drag.

We now estimate the hydrodynamic interactions between 2 rotating ABFs by computing the fluid velocity caused by the rotation of one at the other's location. The magnitude of the velocity caused by the equivalent sphere of radius R rotating with angular velocity ω is given by

$$v_{int}(r) = \omega R^3 / r^2. \quad (6)$$

This rough estimate, at a distance $r = 10a$ (5 body lengths), gives a flow velocity of about $v_{int} \approx 0.12 \mu\text{m s}^{-1}$. ABFs are able to swim at velocities of around one body length per second, that is $v \approx 10 \mu\text{m s}^{-1}$. Hence the velocity due to the interactions amounts to about 1.2% of the swimming velocity when the swimmers are close to each other. This velocity decreases further when the swimmers are separated by larger distances (0.03% when they are separated by 10 body lengths), which is the most common configuration in the current problem. We therefore neglect the hydrodynamic interactions between ABFs in our simulations.

II. FORWARD SLIP

As explained in the main text, the velocity of an ABF subjected to a uniform magnetic field rotating at constant frequency first increases linearly (its rotation follows that of the magnetic field, hence its velocity is constant). After the frequency of rotation of the field reaches the critical value ω_c , the hydrodynamic forces that would be needed to follow the magnetic field frequency are too high, causing the ABF to “slip”. This can be seen on fig. 1. Below ω_c , the velocity is constant, hence the displacement of the ABF increases linearly with time. For higher magnetic field frequency, the ABF slips and hence perform a back and forth motion. The time averaged velocity hence decreases.

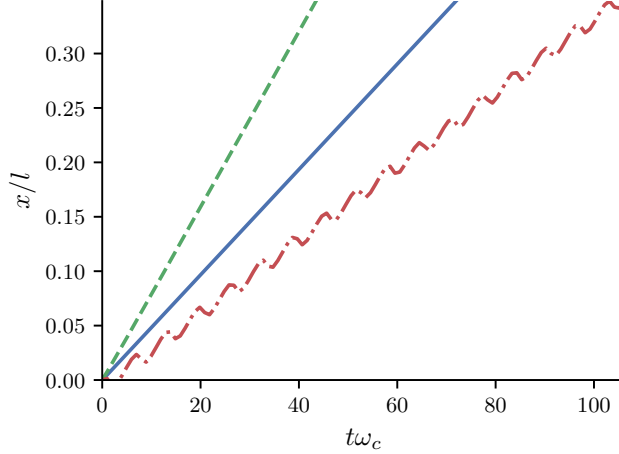


FIG. 1. Displacement (in body lengths l) of an ABF against dimensionless time (w_c is the step out frequency) subjected to a constant rotating magnetic field, with frequency $\omega = 0.6\omega_c$ (—), $\omega = \omega_c$ (- - -) and $\omega = 1.4\omega_c$ (- · - ·).

III. QUATERNIONS

Quaternions are useful mathematical tools to represent rotations in 3 dimensions [3]. Unlike the rotation matrices, which have 9 components in 3 dimensions, quaternions store only 4 components, which make them also desirable on a computational point of view. A quaternion q can be represented as

$$q = q_w + q_x i + q_y j + q_z k, \quad (7)$$

where $q_w, q_x, q_y, q_z \in \mathbf{R}$ are real numbers and $i^2 = j^2 = k^2 = ijk = -1$. A common notation is to decompose the quaternion into a scalar part and a vector part,

$$q = (q_w, \mathbf{q}), \quad (8)$$

where $\mathbf{q} = (q_x, q_y, q_z)$. A quaternion with zero scalar part is called a pure vector quaternion, and a quaternion with the null vector is called a pure scalar quaternion. The conjugate of q is defined as $q^* = (q_w, -\mathbf{q})$. Furthermore, the norm of a quaternion is

$$|q| = \sqrt{q_w^2 + q_x^2 + q_y^2 + q_z^2}. \quad (9)$$

The product between two quaternions, noted \otimes , can be derived from the properties of i, j, k . In vector notations, it is given by

$$q \otimes p = (q_w p_w - \mathbf{q} \cdot \mathbf{p}, q_w \mathbf{p} + p_w \mathbf{q} + \mathbf{q} \times \mathbf{p}), \quad (10)$$

where \times denotes the vector product. Rotations can be represented by unit quaternions $|q| = 1$. The rotation of angle ϕ around the unit vector \mathbf{u} is represented by the quaternion

$$q = \left(\cos \frac{\phi}{2}, \sin \frac{\phi}{2} \mathbf{u} \right). \quad (11)$$

The rotation of a vector \mathbf{x} by q is given in terms of quaternion product,

$$\mathbf{y} = q^* \otimes x \otimes q, \quad (12)$$

where $x = (0, \mathbf{x})$ is the pure vector quaternion of \mathbf{x} and \mathbf{y} is the result of the rotation on \mathbf{x} .

The same operation can be written in matrix form,

$$\mathbf{y} = R(q)\mathbf{x}, \quad (13)$$

where $R(q) = E(q)G^T(q)$ with

$$E(q) = \begin{pmatrix} -q_x & q_w & -q_z & q_y \\ -q_y & q_z & q_w & -q_x \\ -q_z & -q_y & q_x & q_w \end{pmatrix}, \quad (14)$$

$$G(q) = \begin{pmatrix} -q_x & q_w & q_z & -q_y \\ -q_y & -q_z & q_w & q_x \\ -q_z & q_y & -q_x & q_w \end{pmatrix}. \quad (15)$$

IV. CALIBRATION OF THE PROPULSION MATRIX FROM DISSIPATIVE PARTICLE DYNAMICS

The mobility matrix presented in the main text links the external forces and torques applied to a rigid body with its instantaneous linear and angular velocities, relatively to the flow:

$$\begin{bmatrix} \mathbf{V}^b \\ \boldsymbol{\Omega}^b \end{bmatrix} = \begin{bmatrix} \Delta & Z \\ Z^T & \Gamma \end{bmatrix} \begin{bmatrix} \mathbf{F}^b \\ \mathbf{T}^b \end{bmatrix}. \quad (16)$$

The elements of this mobility matrix depend on the shape of the body. In this work, we estimated the mobility matrix of ABFs of different pitch but with the same length and diameter. The body was immersed in a fluid at rest and subjected to rotations and translations with constant speed, and the hydrodynamic torques and forces were collected.

The flow solver, *Mirheo* [4], employs the dissipative particle dynamics (DPD) method [5], that we briefly summarize here for completeness. The flow is discretized into n particles of mass, positions and velocities m_i , \mathbf{r}_i and \mathbf{v}_i , respectively, with $i = 1, 2, \dots, n$. We consider particles with the same mass, $m_i = m$. They evolve in time according to Newton's law of motion,

$$\frac{d\mathbf{r}_i}{dt} = \mathbf{v}_i, \quad (17a)$$

$$\frac{d\mathbf{v}_i}{dt} = \frac{1}{m_i} \mathbf{f}_i, \quad (17b)$$

where \mathbf{f}_i is the total force acting on the i^{th} particle,

$$\mathbf{f}_i = \sum_{j \neq i} \mathbf{f}_{ij}^C + \mathbf{f}_{ij}^D + \mathbf{f}_{ij}^R, \quad (18)$$

$$\mathbf{f}_{ij}^C = aw(r_{ij})\mathbf{e}_{ij}, \quad (19)$$

$$\mathbf{f}_{ij}^D = -\gamma w_D(r_{ij}) (\mathbf{e}_{ij} \cdot \mathbf{v}_{ij}) \mathbf{e}_{ij}, \quad (20)$$

$$\mathbf{f}_{ij}^R = \sigma \xi_{ij} w_R(r_{ij}) \mathbf{e}_{ij}, \quad (21)$$

where $\mathbf{r}_{ij} = \mathbf{r}_i - \mathbf{r}_j$, $r_{ij} = |\mathbf{r}_{ij}|$, $\mathbf{e}_{ij} = \mathbf{r}_{ij}/r_{ij}$ and $\mathbf{v}_{ij} = \mathbf{v}_i - \mathbf{v}_j$. Furthermore, a , γ and σ are the conservative, dissipative and random force coefficients, respectively. ξ_{ij} is a random variable with zero mean and unit variance satisfying

$$\langle \xi_{ij}(t) \rangle = 0,$$

$$\langle \xi_{ij}(t) \xi_{kl}(t') \rangle = (\delta_{ik} \delta_{jl} + \delta_{il} \delta_{jk}) \delta(t - t').$$

The kernel $w(r) = \max(1 - r/r_c, 0)$ vanishes after the cutoff radius r_c . The dissipative and random kernels are linked through the fluctuation-dissipation theorem

$$\sigma^2 = 2\gamma k_B T, \quad (22a)$$

$$w_D = w_R^2, \quad (22b)$$

where $k_B T$ is the temperature of the fluid in energy units. We set $w_D = w^s$ with $s = 1/4$.

The ABF is modeled as a rigid object consisting of frozen DPD particles that move as a rigid body and interact with the surrounding solvent particles. Furthermore, to enforce no-slip and no-penetrability boundary conditions, the solvent particles are bounced back from the surface of the ABF.



FIG. 2. The geometries of the two ABF for which the propulsion matrix has been calibrated. In arbitrary units, the left one has a pitch of 2 and the right one has a pitch of 5. The arrow represents the magnetic moment \mathbf{m} of the ABFs.

The ABFs were first oriented along their principal axes and we assumed that the matrices Δ , Z and Γ had non zero elements only on their diagonal. For each ABF, we perform 6 simulations: in each simulation, only one of the 6 components of the linear and angular velocities, \mathbf{V} and $\mathbf{\Omega}$, is non zero. The time averaged forces and torques were collected for each of these simulations, \mathbf{F}^i and \mathbf{T}^i , where $i = 1, 2, \dots, 6$ is the simulation index. The coefficients of the mobility matrix are then estimated as

$$\Delta_{ii} = V_i^i / F_i^i, \quad (23)$$

$$\Gamma_{ii} = \Omega_i^{i+3} / T_i^{i+3}, \quad (24)$$

for $i = 1, 2, 3$. The coefficient Z_{11} , on the other hand, is computed from the simulation of a freely translating ABF with an imposed rotation with constant angular velocity Ω along its swimming direction in a DPD fluid. After reporting the averaged swimming velocity V , we obtain

$$Z_{11} = \frac{V}{\Omega} \Gamma_{11}. \quad (25)$$

We report the coefficients of the propulsion matrix in dimensionless form $\Delta^* = \Delta \eta l$, $Z^* = Z \eta l^2$ and $\Gamma^* = \Gamma \eta l^3$, where η is the dynamic viscosity of the fluid and l is the length of the ABF. The DPD simulations are run with a Reynolds number $\text{Re} = 0.2$ and a Mach number $\text{Ma} = 0.05$ in a periodic domain of size $10l \times 10l \times 10l$ with the ABFs shown on fig. 2. The nondimensional propulsion coefficients are reported in table I.

We choose the magnetic moment such that the maximum velocity of the swimmer equals one body length per second, which is a typical value found in experiments for a magnetic field of the order of 1 mT. This constraint is expressed as $V_{max} = Z_{11} m B$, hence we set

$$m = \frac{V_{max}}{Z_{11} B}. \quad (26)$$

Pitch	Δ_{11}^*	Δ_{22}^*	Δ_{33}^*	Z_{11}^*	Γ_{11}^*	Γ_{22}^*	Γ_{33}^*
2	0.36	0.32	0.32	0.096	11.9	1.7	1.7
5	0.41	0.37	0.37	0.39	18.2	2.42	2.42

TABLE I. Non dimensional coefficients of the propulsion matrix obtained from DPD simulations with the two geometries shown on fig. 2.

V. REINFORCEMENT LEARNING

The reinforcement learning (RL) method consists in an agent controlling the magnetic field through an action $\mathbf{A} = (a_\omega, a_x, a_y, a_z)$. This action sets the frequency and direction of the rotating magnetic field for Δt simulation time. The angular velocity is set to $\omega = a_\omega$ and the direction is set to $\mathbf{u} = (a_x, a_y, a_z) / \sqrt{a_x^2 + a_y^2 + a_z^2}$. Every Δt time, the environment returns its state \mathbf{s} and reward r to the agent. The state is composed of all positions and quaternions of the ABFs. Due to the absence of inertia, this state describes the full system. The reward has two components, designed to guide the ABFs towards the target in a minimal time:

$$r_t = g_t - c_t. \quad (27)$$

The first term is designed from reward shaping [6]: it increases if the ABFs come closer to the target,

$$g_t = \phi_{t-1} - \phi_t, \quad (28)$$

$$\phi_t = K_\phi \sqrt{\sum_{i=1}^N \|\mathbf{x}_i(t)\|^2},$$

so that the cumulative reward (we use a discount factor $\gamma = 1$), until the final simulation time T , depends only on the initial conditions if the ABFs reached their goal. The constant K_ϕ in eq. (28) is set such that the sum of the shaping part of the reward over one successful episodes is of the order of 1. Therefore, this part of the cumulative reward does not affect the resulting policy [6]. The second term in eq. (27) is designed to penalize long travel times, $c_t = \Delta t / T_{\max}$. Furthermore, an additional positive term is added to the reward if all ABFs reached the target within the given distance d_{success} . We set this constant to $K_{\text{success}} = 1$. The parameters used for the two-swimmers setup are listed in table II.

We used the off-policy actor-critic algorithm **V-RACER**, implemented in the software

Parameter	Value
Δt	$128.5/\omega_{c,1}$
d_{success}	$2l$
T_{max}	$139l/V$
K_{success}	1
K_{ϕ}	$1/72.3l$
\mathbf{x}_1^0	$(50l, 20l, -5l)$
\mathbf{x}_2^0	$(-10l, 30l, 20l)$
σ	$3l$

TABLE II. Parameters used in the RL setup.

`smarties` [7, 8], with the default parameters.

The number of episodes needed to converge for the RL method is of the order of 2.5×10^4 , as shown on fig. 3. The travel time is first equal to the maximum allowed one (when the RL agent is not able to guide the ABFs towards the target). After about 5000 episodes, the ABFs reach the target and the travel time decreases with the number of training episodes. The travel time converges to a smaller value than that of the semi analytical solution.

-
- [1] L. Zhang, K. E. Peyer, and B. J. Nelson, Lab on a Chip **10**, 2203 (2010).
 - [2] S. Kim and S. J. Karrila, *Microhydrodynamics: principles and selected applications* (Courier Corporation, 2013).
 - [3] B. Graf, arXiv preprint arXiv:0811.2889 (2008).
 - [4] D. Alexeev, L. Amoudruz, S. Litvinov, and P. Koumoutsakos, Comput. Phys. Commun. , 107298 (2020).
 - [5] P. Espanol and P. Warren, EPL (Europhysics Letters) **30**, 191 (1995).
 - [6] A. Y. Ng, D. Harada, and S. Russell, in *ICML*, Vol. 99 (1999) pp. 278–287.
 - [7] G. Novati and P. Koumoutsakos, in *Proceedings of the 36th International Conference on Machine Learning* (2019).
 - [8] G. Novati, L. Mahadevan, and P. Koumoutsakos, Physical Review Fluids **4**, 10.1103/PhysRevFluids.4.093902 (2019).

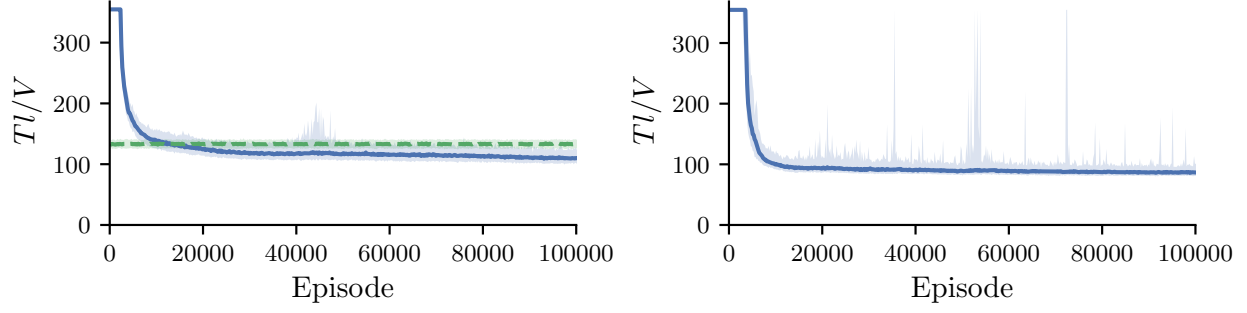


FIG. 3. Dimensionless travel time Tl/V against number of episodes during training obtained with the RL method (—). The left figure corresponds to the case with 2 swimmers and no background flow. The time obtained with the semi-analytical method is shown for comparison (- - -). The right figure corresponds to the case with the background flow. V is the maximum forward velocity of the ABFs and l their length. The line corresponds to the median over 200 episodes, and the shaded area corresponds to the 0.05 and 0.95 quantiles over the same number of episodes.